International Journal of Rock Mechanics & Mining Sciences 80 (2015) 40–50

Contents lists available at ScienceDirect

International Journal of Rock Mechanics & Mining Sciences

journal homepage: www.elsevier.com/locate/ijrmms

Technical Note

Numerical simulation of drilling-induced core damage and its influence on mechanical properties of rocks under unconfined condition

Navid Bahrani [a,b,*], Benoît Valley [c], Peter K. Kaiser [b]

[a] Geomechanics Research Centre, MIRARCO, Sudbury, ON, Canada
[b] Bharti School of Engineering, Laurentian University, Sudbury, ON, Canada
[c] Centre for Hydrogeology and Geothermics, University of Neuchâtel, Neuchâtel, Switzerland

ARTICLE INFO

Article history:
Received 2 June 2014
Received in revised form
2 September 2015
Accepted 4 September 2015
Available online 25 September 2015

Keywords:
Core damage
Stress path
Rock strength
Crack initiation
Crack damage
Particle Flow Code

1. Introduction

At the early stages of deep underground construction projects, data are primarily obtained from boreholes from which strategic decisions are made for the design of underground infrastructures. For this purpose, the unconfined compressive strength (*UCS*) and the Young's modulus (*E*) of intact rock as well as the in situ stress state are obtained as fundamental engineering parameters during the course of geotechnical site characterization. Unfortunately, drilling in relatively high stress environments can induce disturbance, micro-cracking of the cores, which in turn may result in lower rock strength and Young's modulus measured in the laboratory[1] compared to their intact values or affect stress measurement results[2,3]. This may lead to erroneous estimates of design parameters.

While drilling-induced core damage has been recognized for more than fifty years,[4] this early focus was primarily on drilling-induced macro core damage known as core disking and less on understanding the mechanisms involved in the initiation and accumulation of drilling-induced micro damage and its impact on rock properties. In situ evidence of core damage was documented at the Underground Research Laboratory (*URL*) in Manitoba, Canada, by Martin and Stimpson[1] and Eberhardt et al.[5] They showed that the *UCS*, the Young's modulus, and the P-wave velocity measured on cores decrease and the Poisson's ratio increases as rock cores are obtained from increasing depth and consequently increasing in situ stresses. Contrary to the velocity measured on cores, the in-situ velocity from sonic logs appeared to be independent of depth[1] and solely related to macro-fracture density, suggesting that the borehole walls are much less affected by stress-induced micro-damage than the core. A similar behavior was also observed on specimens taken from deep mines in South Africa.[6] Crack counts using Scanning Electron Microscope (*SEM*) analyses support that specimens from greater depths contain larger numbers of micro-cracks. Lanaro et al.[7] reported a strong negative correlation between rock strength and in situ stress, and explained this observation by the core damage. The strength reduction in their case was not only a matter of depth but also related to high stress zones associated with faults. Stress-induced damage was also experimentally investigated by Holt et al.[8] using synthetic rock specimens cured in the laboratory under initial stress. They unloaded the synthetic specimens axially and then laterally to simulate the drilling-induced stress release in a core

* Correspondence to: Department of Civil Engineering, University of Toronto, Galbraith Building, 35 St. George Street, Toronto, ON, Canada M5S 1A4.
E-mail address: navid.bahrani@utoronto.ca (N. Bahrani).

http://dx.doi.org/10.1016/j.ijrmms.2015.09.002
1365-1609/

drilled from a vertical borehole, and found that the strength, stiffness, porosity and elastic wave velocities of the synthetic specimens were permanently reduced as a result of unloading. In some cases disking-type fractures were observed. These results were reproduced numerically[9–12] using calibrated distinct element models that were capable of capturing the damage associated with the drilling-induced stress path as well as the stress memory effects in rocks used for the determination of in situ stresses.

In general terms, the process of drilling-induced core damage is relatively well understood: when a rock core is drilled and retrieved from underground, the state of stress inside the core is changed from the original in situ stresses to the atmospheric condition.[13] Between the initial and end points, the stress path involves changes in orientation and magnitude. Such changes depend on the orientation of the borehole relative to the principal stress directions as well as their magnitudes.[13] The stress path inside the core typically includes an increase of the deviatoric stress in the core, which may generate micro-cracks if the intact rock crack initiation stress is reached or exceeded. Stress concentration and the generated tensile stresses at the contact between the drill bit and the rock may also initiate new micro-cracks,[14] which may in turn result in stress redistribution and propagation of new cracks towards the center of the core.[15,16] The interaction and coalescence of these micro-cracks due to large deviatoric and tensile stresses may result in the formation of macroscopic fractures known as partial (incipient) and full core disking.[17] It has been shown that the borehole orientation relative to the principal stress directions influences the stress paths and associated induced micro-crack patterns and that core disking and core damage are more likely to occur when the boreholes are drilled perpendicular to the maximum principal stress orientation.[2,4]

In this study, an elastic three-dimensional (3D) model based on the finite element method (*FEM*) was used to obtain the drilling-induced coring stress paths for boreholes parallel to the major (σ_1) and minor (σ_3) principal stress directions, within a stress state representative for the 420-level of the *URL* in Manitoba, Canada. The coring stress path for a borehole parallel to the σ_3 direction (vertical borehole) was approximated and applied to a two-dimensional (*2D*) model based on the distinct element method (*DEM*) that was previously calibrated to the mechanical properties of the undamaged Lac du Bonnet (*LdB*) granite. In this manner, damage in the form of micro-cracks was created in the synthetic specimens. The damaged synthetic specimen was then loaded and the input parameters were adjusted to match the properties of undamaged and damaged *LdB* granite. The calibrated synthetic specimen was also used to estimate the amount of damage and the unloading-induced micro-crack characteristics of a core drilled from a borehole parallel to the σ_1 direction (horizontal borehole). The synthetic specimens were then used to investigate the influence of core damage on the laboratory properties of damaged rocks under unconfined condition including the Young's modulus, the unconfined compressive strength, and the crack initiation and crack damage stresses.

2. Method of investigation

Rock fracturing process (crack initiation and propagation) is a three-dimensional phenomenon. Ideally, a three-dimensional simulation of borehole excavation should be conducted to properly consider the process of drilling and recovering a core including the stress path, stress rotation and damage initiation and propagation inside the core. Therefore, a three-dimensional numerical code based on the distinct element method would be an ideal tool, as it is capable of capturing all the pre- and post-peak fracturing processes. However, such a model with a reasonable number of particles would be computationally demanding as numerous runs would be required for model calibration. In this study, two types of numerical modeling methods, namely the finite element method in three dimensions to obtain the 3D coring stress path and the distinct element method in two dimensions to simulate the drilling-induced core damage were used. The mechanical properties of *LdB* granite used for the calibration purposes as well as the modeling approaches and assumptions are discussed in this section.

2.1. Mechanical properties of undamaged and damaged Lac du Bonnet granite

The *URL* is located within the *LdB* batholiths, about 100 km northeast of Winnipeg, Manitoba, Canada. An extensive in situ stress characterization program using different stress measurement techniques identified three distinctive stress domains at the *URL*.[18] Stress Domain 1 extends from surface to a depth of about 200 m. Stress Domain 2 serves as a transition zone between Domains 1 and 3 and is affected by a main fracture zone. Stress Domain 3 extends to the deepest measurement point at 550 m and is located within the massive gray granite. Typical magnitudes of principal stresses for these three domains are given in Table 1. The minimum principal stress is typically sub-vertical.

Martin and Stimpson[1] suggested that the damaged rock cores could be identified from the change in the material response when subjected to uniaxial compression; undamaged specimens from Domain 1 respond in a linear elastic manner, whereas damaged specimens from Domain 3 initially exhibit a strongly non-linear response due to micro-crack closure. These observations were consistent with the results of *SEM* analyses by Eberhardt et al.,[5] who noted that visible cracks were difficult to find in the thin sections of the specimens from Domain 1 and Domain 2, whereas numerous cracks were visible in the specimens from Domain 3. The *UCS* of the undamaged and damaged specimens from vertical boreholes in Domains 1 and 3 are 213 ± 20 MPa and 157 ± 18 MPa (mean $\pm$ 1standard deviation), respectively, and the Young's modulus is 65 ± 5 GPa for undamaged *LdB* granite and 52 ± 2 GPa for the damaged *LdB* granite.[5] The direct tensile strength for undamaged *LdB* granite is 7 ± 1 MPa.[20] Unfortunately, no published data on the tensile strength of damaged *LdB* granite, mechanical properties of the cores obtained from horizontal boreholes and their possible amounts of damage exists.

The damaged specimens taken from the *URL*'s 420-level (Domain 3) were drilled from nearly vertical boreholes (parallel to the σ_3 direction) at depths between 20 and 60 m from the excavation, where the influence of excavation disturbance was minimal.[21] Partial and full core disking were observed in boreholes with depths less than 2.5 m from the excavation.[22] Therefore, the far field in situ stresses representative for Domain 3 (σ_1=60 MPa, σ_2=45 MPa, and σ_3=11 MPa) were used as input to obtained the stress paths from the 3D *FEM* models and simulate core damage (not disking) using the 2D *DEM* models.

Table 1
In situ stress values for the three main domains at the Underground Research Laboratory.

Stress domains	σ_1 (MPa)	σ_3 (MPa)	σ_2 (MPa)	Source
1 (130 m)	14	6	9	Ref. 18
2 (240 m)	30	12	15	Ref. 2
3 (420 m)	60	11	45	Ref. 19

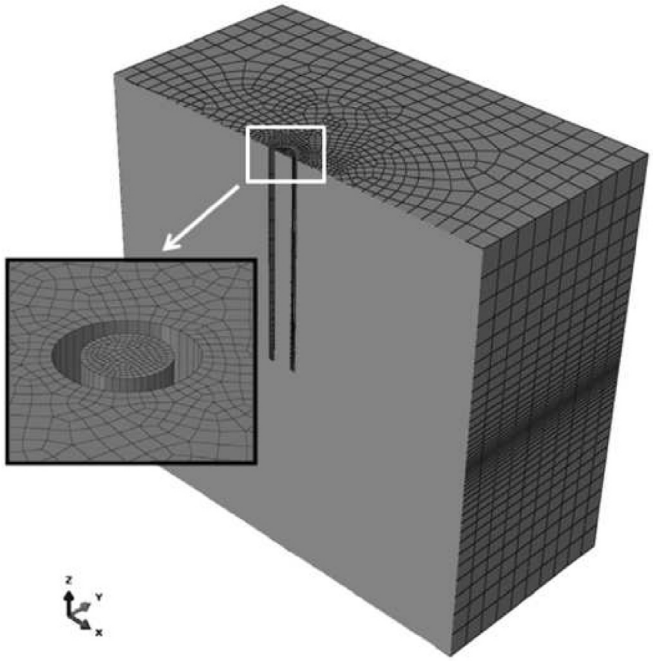

Fig. 1. The three-dimensional (3D) finite element model used for simulation of core drilling. This figure illustrates half of the geometry of the 3D model with a section through the center of model indicating the depth of the borehole, as well as mesh density inside the core and near the borehole wall.

2.2. Three-dimensional FEM model

Three-dimensional elastic analyses were first carried out in order to derive the stress change inside the core during drilling as a function of borehole orientation relative to the in situ principal stress directions. For this purpose, a 1 m × 1 m × 1 m model consisting of 59,440 20-node quadratic brick with reduced integration (C3D20R) was built using the commercially available *FEM* code Abaqus (http://www.simulia.com). Fig. 1 shows a section through the center of the model indicating the depth of borehole and the density of mesh inside the core and near the borehole wall. The simulated core and borehole were 47.6 mm and 75.7 mm in diameter, respectively (i.e., NQ size). Pinned boundary conditions were applied to each model face except for the top face with the borehole access, where rollers were used. A linear elastic material model was used with a Young's modulus of 65 GPa and a Poisson's ratio of 0.25.

The analysis was performed for two borehole orientations: (1) borehole parallel to the direction of the maximum principal stress (σ_1) (or maximum horizontal stress, σ_{Hmax}); and (2) borehole parallel to the direction of the minimum principal stress (σ_3) (or vertical stress, σ_v). The stress change inside the core was computed in a single static step by sampling stress profiles parallel to the borehole axis.

2.3. Two-dimensional DEM model

The micro-scale stress path and micro-crack patterns were studied using the Particle Flow Code in two dimensions, *PFC2D*,[23] which is based on the distinct element method (*DEM*) developed by Cundall[24] and Cundall and Strack.[25] In this approach, brittle rocks are simulated as an assemblage of circular particles, cemented at their contact points.[26] This method, called the Bonded Particle Model (*BPM*), was selected because it explicitly simulates cracking as bond breakage and pre-defined complex empirical constitutive relations are replaced with simpler particle contact logic without requiring plasticity rules. Once a bond breaks, the displacement field, as well as the transition to the residual strength, are controlled by particle geometry and friction at particle–particle contacts. This approach explicitly captures a fundamental characteristic of brittle failing rocks known as the cohesion weakening frictional strengthening process.[27,28] Theoretical aspects of the *BPM* in *PFC* have been described by Potyondy and Cundall,[26] Holt et al.[29] and Cho et al.,[30] and are not repeated here.

Various approaches in *PFC2D* to simulate brittle failing rocks have been proposed, since the initial approaches were not able to capture some of the characteristics of brittle failing rocks such as the tensile to compressive strength ratio, the non-linear failure envelope as well as realistic friction angle.[26,30,31] The clumped particle modeling (*ClmPM*) approach proposed by Cho et al.[30] was chosen for this study. A clump consists of multiple circular particles that are glued together in order to behave as a single rigid object. This approach generates irregular shaped particles (similar to grains), leading to a more realistic kinematic behavior than using circular shaped particles. With this method, models have been successfully calibrated to the mechanical properties of intact *LdB* granite, including the tensile to uniaxial compressive strength ratio.[30] The synthetic specimen generated following the approach proposed by Cho et al.[30] is called the “clumped specimen” in this paper.

The procedure for generating a clumped specimen has been described by Cho et al.[30] and Yoon et al.[32] and is not repeated here. For this study, a 3.17 cm × 6.34 cm synthetic specimen was generated with circular particles in *PFC2D* and then converted to a *ClmPM*. The average clump size (diameter) of 2 mm was chosen to be close to the average grain size of *LdB* granite. A total of 6 models with different particle seeds were generated and the average values of the simulation test results were compared with those of laboratory test results. The clump generation process, as well as the application of bonds between the clumps, were done at nearly zero initial stress (i.e., 0.1 MPa) prior to bringing the synthetic specimens to the in situ stress magnitudes representative for the 420-level of the *URL*. No bond breakage occurred during the clump generation and stress initialization stages. The following steps were used to calibrate the clumped specimens to the properties of both undamaged and damaged *LdB* granite.

Calibration to undamaged properties: the clumped specimen was first calibrated to the direct tensile and uniaxial compressive strengths, as well as the Young's modulus of undamaged *LdB* granite.

Calibration to damaged properties: once the clumped specimen was calibrated to the properties of undamaged *LdB* granite, it was loaded to the initial in situ stresses (σ_1 = 60 MPa, σ_3 = 11 MPa) using the standard stress initialization procedure in *PFC*. An approximate coring stress path was applied to the clumped specimen to create damage in the form of micro-cracks inside the specimen (this will be discussed in Section 3.1). The damaged clumped specimen was then reloaded uniaxially and the uniaxial compressive strength and the Young's modulus were compared to those of damaged *LdB* granite retrieved from the nearly vertical boreholes from the 420-level of the *URL*. If a match with the properties of damaged *LdB* granite could not be achieved, the calibration had to be redone from step one.

Once a set of parameters was found that was in agreement with all the target macro-properties (i.e., properties of undamaged and damaged *LdB* granite), the process was stopped. Note that since there are more independent input parameters than independent constraints the resulting solution is not unique.

3. Results of core damage modeling

3.1. Macro-scale stress path

The stress paths of eight points inside the core tracked during drilling simulation using the 3D *FEM* model are shown in Fig. 2 and highlight non-uniform stress changes during drilling for the two borehole orientations. This is consistent with the results obtained by Lim and Martin[22] who investigated the stress paths of three points inside the core for the case of a vertical borehole. Point 1 (P1) and point 8 (P8) in Fig. 2 are located in the center and at the wall of the core, respectively. The other six points are located between these two points within a 3 mm distance from each other. These points are located parallel and perpendicular to one of the principal stress directions on a plane perpendicular to the borehole axis. As can be seen from Fig. 2, the points in the center and at the wall of the cores experience the lowest and highest tensile stresses, respectively.

The initial stresses are compressive and the cores in the two cases experience a gradual reduction in σ_3 and σ_1. In the case of the borehole parallel to the σ_3 direction (Fig. 2a), the value of σ_1 first increases from 60 MPa to about 70 MPa, and then decreases back to 60 MPa when the core is in tension with the maximum

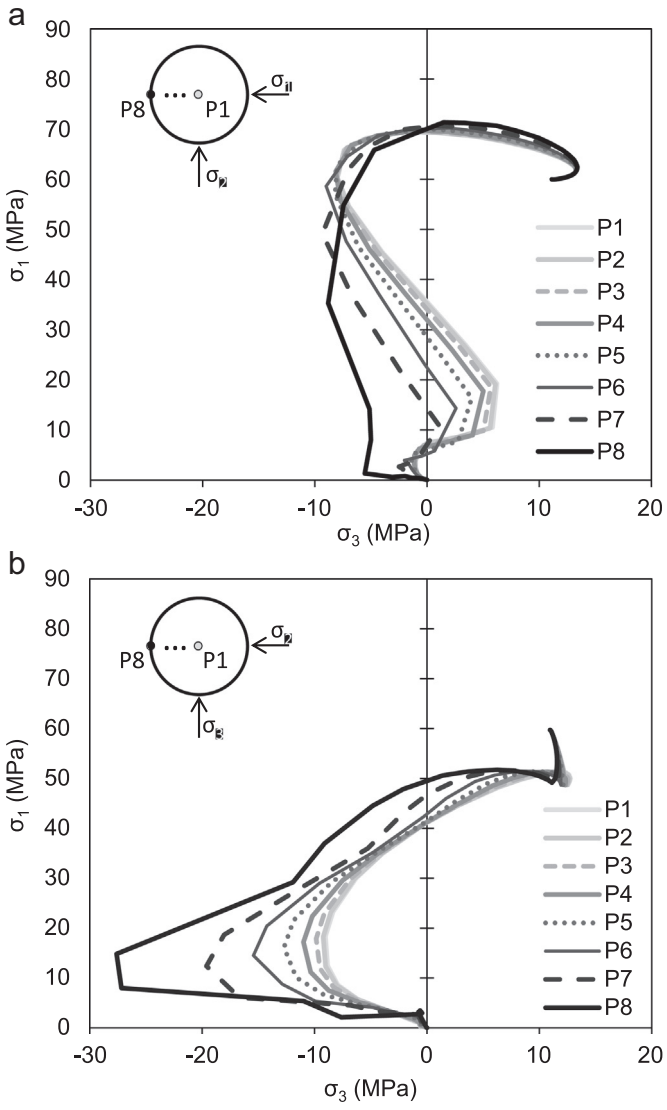

Fig. 2. Coring stress paths of the points inside the core for: (a) borehole parallel to the σ_3 direction; and (b) borehole parallel to the σ_1 direction.

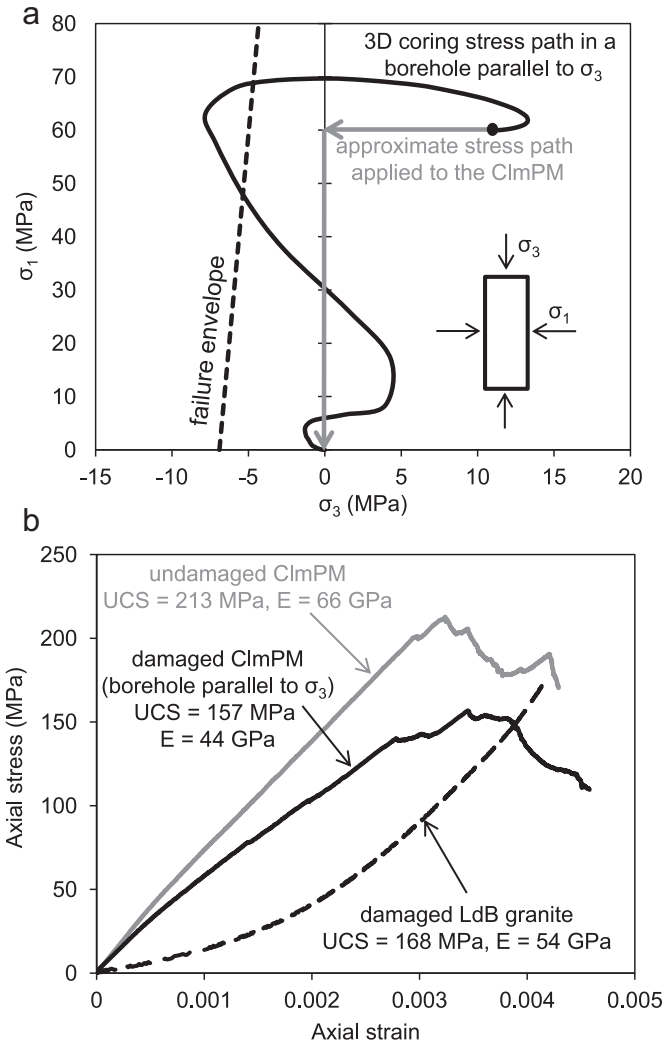

Fig. 3. (a) 3D coring stress path in a borehole parallel to the σ_3 direction from the 3D *FEM* model and approximate coring-induced stress path applied to the clumped particle model. The failure envelope of the undamaged *LdB* granite from laboratory test results passing through its average direct tensile strength is also shown with the dashed line; (b) comparison between the stress–strain curves of the undamaged and damaged clumped specimens after applying the approximate stress path of a core drilled from a borehole parallel to the σ_3 direction and the stress–strain curve measured on a damaged *LdB* granite specimen (dashed line).

tensile stress exceeding the average direct tensile strength of the undamaged *LdB* granite. In the case of the borehole parallel to the σ_1 direction (Fig. 2b), the value of σ_1 is first reduced from 60 MPa to about 50 MPa. The confinement is then gradually removed from the core and reaches zero when σ_1 is nearly 40 MPa. From this point the tensile stress increases and passes the average direct tensile strength of the undamaged *LdB* granite.

The stress paths shown in Fig. 2 were then simplified by taking the median value of the stress paths of all the points inside the core (black curves in Fig. 3a and Fig. 4a). The stress path applied to the clumped specimen is shown in Fig. 3a. As can be seen from this figure, this stress path is an approximation of the 3D elastic stress path, and only captures the unloading that occurs under an overall compressive stress field, but not the one that goes to the tensile zone. This approximation was needed as it was found during the calibration process that it is not possible to match both the tensile and compressive strengths of *LdB* granite by applying an unloading stress path that starts from the compressive zone and then goes to the tensile zone; the damaged clumped specimen would fail in the tensile zone before the stress path reaches the failure envelope of

Table 2
Micro-properties of the calibrated clumped particle model.

Parameter	Symbols	Values
Minimum particle radius	R_{min}	0.2 mm
Ratio of maximum to minimum particle radius	R_{max}/R_{min}	1.5
Contact and parallel bond stiffness ratios (normal to shear)	k_n/k_s and $\bar{k}^n/\bar{k}^s$	2.5
Contact bond moduli	E_c	15 GPa
Parallel bond moduli	$\bar{E}_c$	18 GPa
Particle friction coefficient	μ	0.3
Parallel bond radius multiplier	$\bar{\lambda}$	1
Parallel bond normal strength	$\bar{\sigma}_n$	12 ± 1.2 MPa
Parallel bond shear strength	$\bar{\sigma}_s$	155 MPa
Clump radius	R_{cl}	1 ± 0.2 mm

undamaged *LdB* granite. This is interpreted to be due to the large amounts of micro-cracks generated during unloading in the compressive zone. Note that the cores of *LdB* granite retrieved from vertical boreholes were solid and did not fail in tension and only contained micro-cracks.[5,22] Therefore, in order to capture the micro-cracks and avoid pre-mature failure of the specimen, only the stress path under the compressive stress field was considered for the calibration process. This approximated stress path is similar to that used by Holt et al.,[8] who simulated drilling-induced core damage and core disking in their laboratory tests.

3.2. Clumped particle model calibration results

Table 2 lists the micro-properties obtained from the described calibration procedure for the case of the borehole parallel to the σ_3 direction. Note that no standard deviation was assigned to the bond strength parameters. Therefore, geometry heterogeneity (different shape and size of clumps) is the only source of heterogeneity, which causes variability in the results of numerical simulations. A comparison of the macro-properties obtained from tests simulated on the clumped specimens and laboratory test results of undamaged and damaged *LdB* granite is presented in Table 3. The results indicate an agreement between the laboratory tests and numerical simulations for both the mean values and their standard deviations.

The stress–strain curves of the undamaged and damaged clumped specimens (from the stress path in Fig. 3a) and the stress–strain curve of the damaged *LdB* granite from laboratory tests is shown in Fig. 3b. Although the reduced strength (average *UCS*=157 MPa) and Young's modulus (average *E*=44 GPa) were properly captured, the damaged clumped specimen fails to capture the initial non-linear portion of the stress–strain curve observed in the stress–strain curve of the damaged *LdB* granite specimens (dashed line in Fig. 3b). This is because crack opening during unloading and thus crack closure while reloading was not captured in the numerical simulations (i.e., the clumped specimen is cracked but the cracks do not open, which means that the clumps are still in contact after bond breakage).

Once the models were calibrated to both undamaged and damaged properties of *LdB* granite (with simulated coring-induced stress path for the borehole parallel to the σ_3 direction), an approximate stress path relevant for the core retrieved from a borehole parallel to the σ_1 direction (i.e., horizontal borehole) was applied to the undamaged clumped specimen as shown in Fig. 4a. Fig. 4b compares the stress–strain curves of the undamaged and damaged clumped specimens (from the stress path in Fig. 4a) and the stress–strain curve of the undamaged *LdB* granite from laboratory tests (dashed line). Fig. 4b shows that the stress–strain curves prior to the peak stress as well as the calculated *UCS* and *E* of the two clumped specimens are essentially identical and very similar to those of undamaged *LdB* granite.

Table 3
Comparison between laboratory and *PFC* simulation test results for undamaged and damaged *LdB* granite. *LdB* laboratory test results were extracted from Refs. 20,5 and 22.

Parameter	Lab test results	PFC results
Undamaged *UCS* (MPa)	213 ± 20	212 ± 13
Undamaged *E* (GPa)	65 ± 5	65 ± 3
Undamaged σ_t (MPa)	7 ± 1	7.2 ± 0.2
Damaged *UCS* (MPa)	157 ± 18	158 ± 18
Damaged *E* (GPa)	52 ± 2	48 ± 3

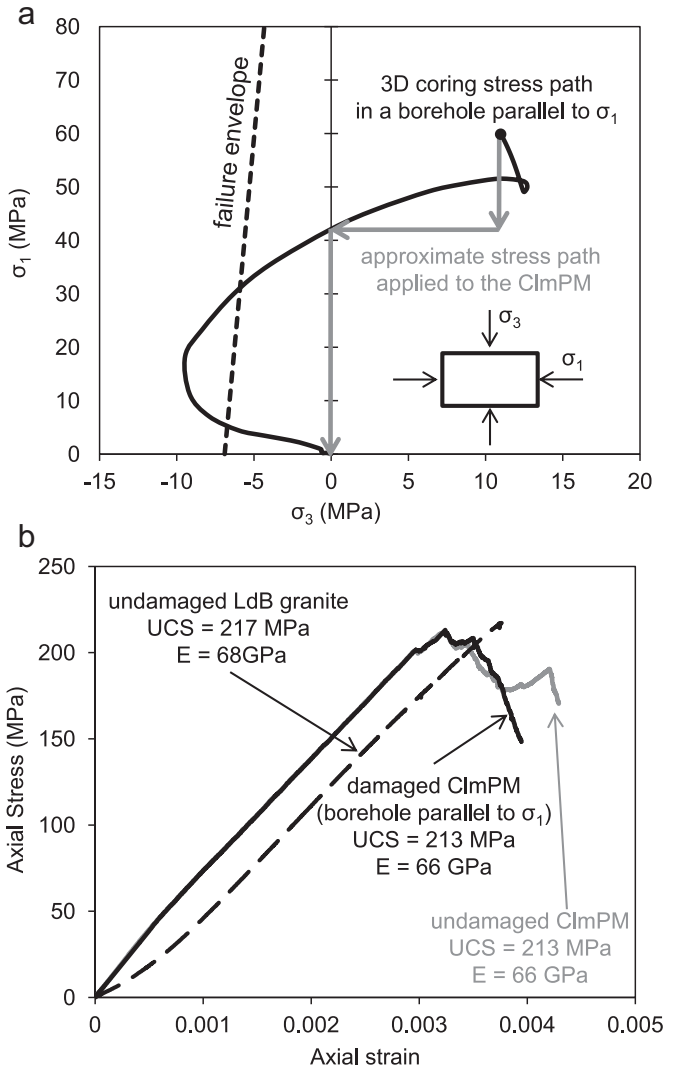

Fig. 4. (a) 3D coring stress path in a borehole parallel to the σ_1 direction from the 3D *FEM* model and approximate coring-induced stress path applied to the clumped particle model. The failure envelope of the undamaged *LdB* granite passing through its average direct tensile strength is also shown with dashed line; (b) comparison between the stress–strain curves of the undamaged and damaged clumped specimens after applying the approximate stress path of a core drilled from a borehole parallel to the σ_1 direction and the stress–strain curve measured on an undamaged *LdB* granite specimen (dashed line).

3.3. Micro-scale stress paths

In order to gain more insight into the evolution of stresses within the damaged specimens during the applied unloading–loading cycle, a grid of 105 measurement circles were placed inside the clumped specimens. The radius of measurement circles

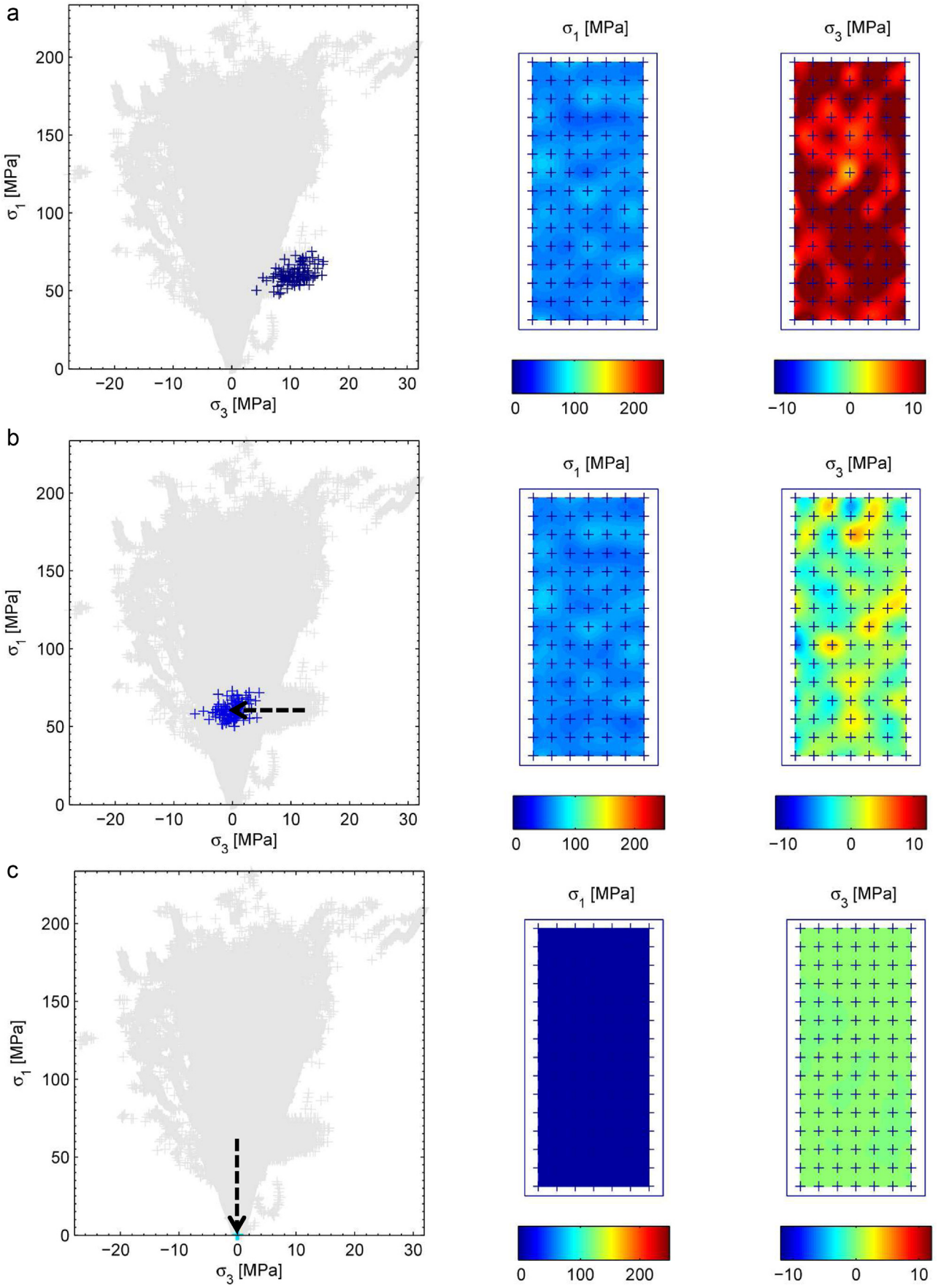

Fig. 5. Evolution of stresses inside the simulated core drilled from the borehole parallel to the σ_3 direction during the unloading stages. The average stresses are: (a) $\sigma_1 = 60$ MPa, $\sigma_3 = 11$ MPa; (b) $\sigma_1 = 0$ MPa, $\sigma_3 = 11$ MPa; and (c) $\sigma_1 = 0$ MPa, $\sigma_3 = 0$ MPa. In the σ_1 versus σ_3 space plots, the black crosses are the stresses at the current state and the gray background indicates all the stresses monitored over the entire unloading and loading processes. The black dashed arrows show the applied macroscopic stress paths.

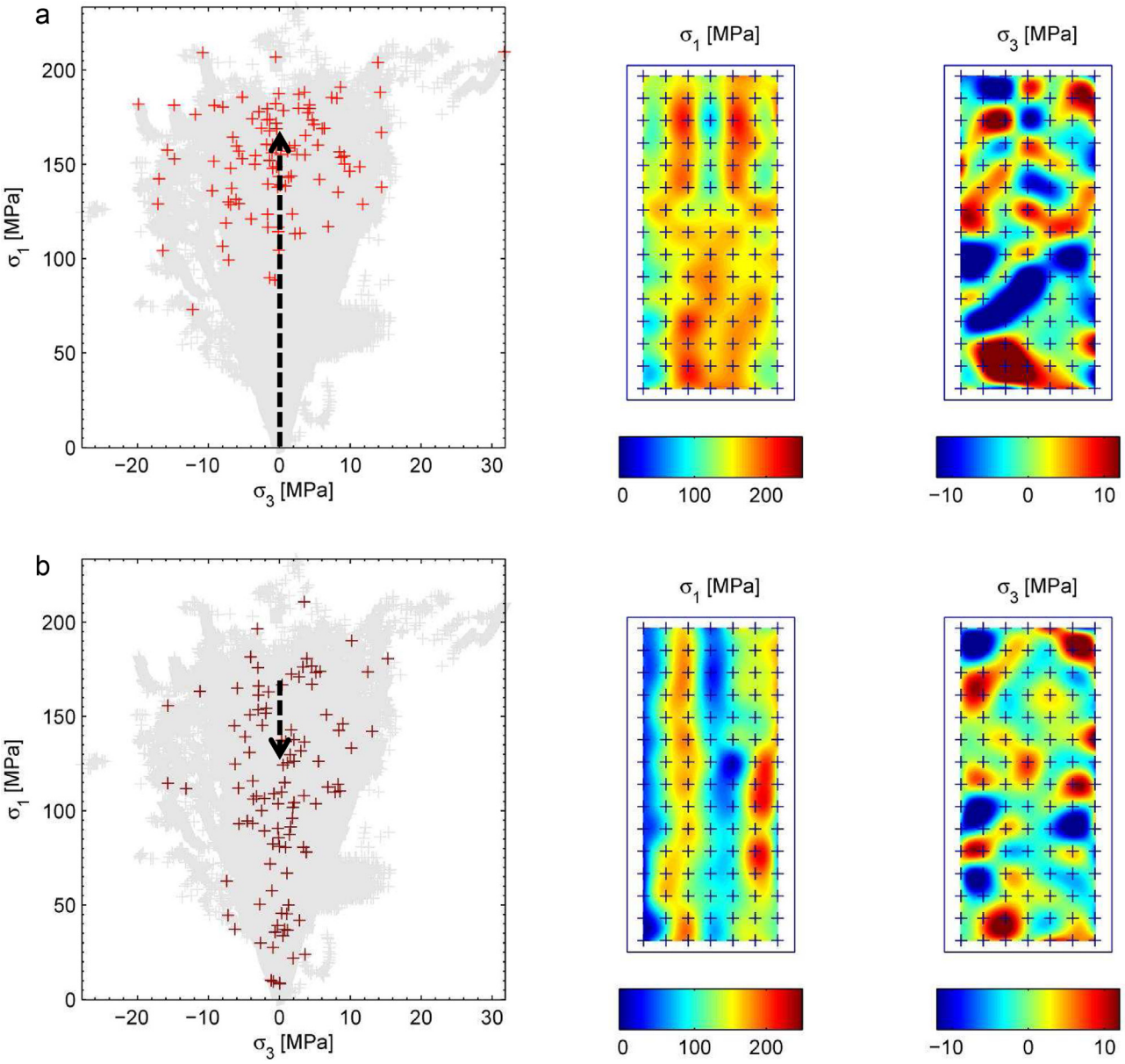

Fig. 6. Evolution of stresses inside the simulated core drilled from borehole parallel to the σ_3 direction during the loading stages. The average stresses are: (a) $\sigma_1 = 157$ MPa, $\sigma_3 = 0$ MPa; and (b) $\sigma_1 = 126$ MPa, $\sigma_3 = 0$ MPa. In the σ_1 versus σ_3 space plots, the black crosses are the stresses at the current state and the gray background indicates all the stress values monitored over the entire unloading and loading process. The black dashed arrows show the applied macroscopic stress paths.

was set to two times the average clump radius. The stress components of each measurement circle were retrieved every 100 time steps during the calculation.

Figs. 5 and 6 present the evolution of grain-scale stresses in σ_1 versus σ_3 space and contours of σ_3 and σ_1 during unloading and loading stages with the simulated coring stress path representative for the borehole parallel to the σ_3 direction. The applied macroscopic stress paths are shown with the dashed lines in these figures. Stage 1, shown in Fig. 5a, corresponds to the stress state at the beginning of the simulation, just after stress initialization. The overall stress state calculated from the walls in the clumped specimen corresponds to the in situ stress state at Domain 3 of the *URL*. The scatter from the mean value (i.e., applied macroscopic stress path) is noticeable with a range of ± 5 MPa for σ_3 and ± 15 MPa for σ_1. This initial stress heterogeneity is a result of the stress initialization procedure, wherein the clumped specimen is compacted until the target stress magnitudes are obtained. Within the specimen, local adjustments of the clumps due to their geometric heterogeneities generate the observed stress scatter. Such an initial stress heterogeneity is critical for damage development during unloading. At Stage 2, in the case of the borehole parallel to the σ_3 direction (Fig. 5b), when the axial load is gradually removed, a stress dispersion similar to the initial stage remains, rendering about half of the clumped specimen in the tensile zone. The tensile stresses are not concentrated, promoting damage throughout the clumped specimen, with the number of tensile micro-cracks depending on the magnitude of the generated tensile stresses. At Stage 3 (Fig. 5c), the clumped specimen is entirely relaxed and all the stress components are zero.

During loading of the now damaged clumped specimen (Fig. 6), the same phenomenon occurs as during the stress initialization stage; local adjustment of the rigid and irregular shaped clumps due to their geometric heterogeneity promotes stress dispersion and tensile conditions under an overall compressive setting. The stress dispersion is much wider compared to the pre-peak stages with a range of ± 17 MPa for σ_3 and ± 75 MPa for σ_1. With

increasing the axial load, the stress pattern within the clumped specimen promotes the formation of columns of high and low stresses (called stress channels), which occur at the peak stress in the top center of the damaged clumped specimen (Fig. 6a). In the post-peak stage (Fig. 6b), the stress channels become organized and propagate with a low magnitude of σ_1 through the center of the damaged clumped specimen. A similar behavior was also observed in the damaged clumped specimen with the simulated coring stress path for the borehole parallel to the σ_1 direction.

Two video files are provided in the electronic version of this paper, which show the evolution of grain scale stresses during unloading and reloading stages of the two models, similar to those shown in Fig. 5 and Fig. 6; Video 1 for the simulated core retrieved from the borehole parallel to the σ_3 direction (vertical borehole), and Video 2 for the simulated core retrieved from the borehole parallel to the σ_1 direction (horizontal borehole). These video files contain: (1) a graph showing the maximum and minimum principal stresses and the number of cracks as a function of numerical step (Video 1a and Video 2a); (2) a graph showing the evolution of stresses on a σ_1 versus σ_3 space (Video 1b and Video 2b); (3) contours of σ_1 (Video 1c and Video 2c); and (4) contours of σ_3 (Video 1c and Video 2c).

Supplementary material related to this article can be found online at: http://dx.doi.org/10.1016/j.ijrmms.2015.09.002

3.4. Evolution of micro-cracks

3.4.1. Cracking during unloading stages

Fig. 7a and c shows the stresses calculated at the clumped specimen boundaries (walls) as well as the number of micro-cracks formed during the unloading stages for the two cases explained above. In the case of the borehole parallel to the σ_3 direction (Fig. 7a), the unloading process can be divided into two main stages. During the first stage, the value of σ_3 is reduced from 11 MPa to zero. As illustrated in Fig. 7a, the number of micro-cracks increases with increasing the deviatoric stress. This is consistent with the laboratory test results on synthetic sandstone reported by Holt et al.[8] In the second stage, the value of σ_1 is gradually reduced to zero. No micro-cracks were developed during this stage. In the case of the borehole parallel to the σ_1 direction (Fig. 7c), the value of σ_1 is first reduced from 60 MPa to 40 MPa and the value of σ_3 is then reduced to zero from its original value of 11 MPa. At this stage, cracks start to grow with increasing the deviatoric stress, once the vertical stress falls below 5 MPa

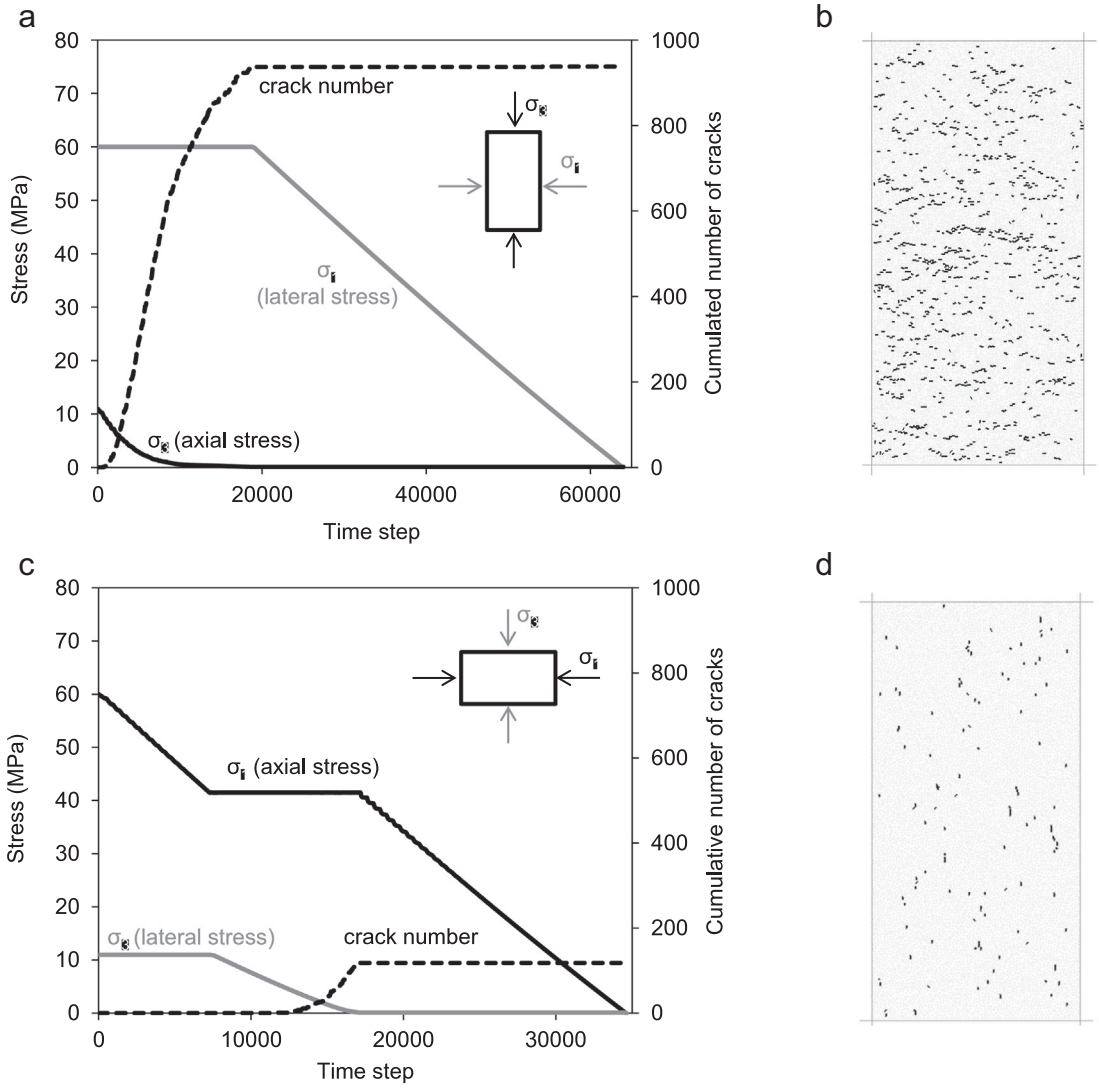

Fig. 7. (a) Unloading process and (b) accumulated micro-cracks inside the clumped specimens simulating drilling-induced core damage that occurs in a borehole parallel to the σ_3 direction; (c) unloading process and (d) accumulated micro-cracks inside the clumped specimens simulating drilling-induced core damage that occurs in a borehole parallel to the σ_1 direction. Note that all the micro-cracks generated during the unloading stages are tension cracks.

(deviatoric stress of 35 MPa). In the last stage, the value of σ_1 is gradually reduced until the specimen reaches the atmospheric stress state with no further crack growth. Once the stresses were reduced to the atmospheric stress state, the lateral walls were removed and the damaged clumped specimens were loaded axially to obtain the *UCS* and Young's modulus.

Fig. 7b and d compares the micro-crack patterns generated inside the clumped specimens during the unloading stages for the boreholes parallel to the σ_3 and σ_1 directions, respectively. As can be seen from these figure, unloading induces tensile micro-cracks that are randomly located in both specimens with the orientations of these cracks being nearly perpendicular to the specimen axis for the borehole parallel to the σ_3 direction (Fig. 7b), and parallel to the specimen axis for the borehole parallel to the σ_1 direction (Fig. 7d). Visual comparison between Fig. 7b and d, in terms of the number of micro-cracks, suggests that the core retrieved from the vertical borehole (i.e., borehole parallel to the σ_3 direction) is more damaged and therefore expected to be weaker and softer compared to the core retrieved from the horizontal borehole (i.e., borehole parallel to the σ_1 direction). This was reproduced when reloading the damaged clumped specimens (see Fig. 3b and Fig. 4b).

3.4.2. Cracking during loading stages

Fig. 8a and b shows the stresses calculated at the model boundaries (walls) as well as the number of micro-cracks formed due to axial loading of the clumped specimens damaged after the application of the coring stress paths for the boreholes parallel to the σ_3 and σ_1 directions, respectively. In both cases, tensile cracks are generated at a very low axial stress. The number of tensile cracks increases rapidly with increasing axial stress. The rate of tensile crack growth decreases from about 50% to 80% of the peak axial stress. During this period the high degree of interlock between the unbreakable clumps causes the clumped specimen to accept more axial stress until shear cracks are generated at about 80% and 90% of the peak axial stresses for the damaged specimens with the coring stress paths of the boreholes parallel to the σ_3 and σ_1 directions, respectively. These shear cracks, although small in quantity, are essential in driving the synthetic specimens to failure, as they interact with the previously generated tensile cracks, and this eases the generation of stress channels through the specimens as well as the kinematic freedom of the clumps.

The locations, orientations and modes (shear or tensile) of all micro-cracks formed in the clump specimens from the beginning of the unloading stage to the end of axial loading (70% of the peak strength in the post-peak region), in the cases of the boreholes parallel to the σ_3 and σ_1 directions are illustrated in Fig. 9a and b, respectively. The micro-cracks in the case of the borehole parallel to the σ_1 direction are mainly oriented sub-parallel to the specimen axis (Fig. 9b), whereas the micro-cracks with orientations parallel and perpendicular to the specimen axis can be seen in the case of the borehole parallel to the σ_3 direction (Fig. 9a). The interaction between the micro-cracks perpendicular to the specimen axis generated during the unloading stage in the case of the borehole parallel to the σ_3 direction (i.e., vertical borehole) with those parallel to the specimen axis, formed during axial reloading, resulted in the failure of the specimen at a lower stress, compared to the case of the simulated core from the borehole parallel to the σ_1 direction.

3.5. Compressive failure process

Four stages in the stress–strain curves of brittle rocks, including crack closure, elastic region, stable crack growth and unstable cracking have been described by Martin.[20] The crack closure (Stage 1) may or may not be present in laboratory tests depending on the

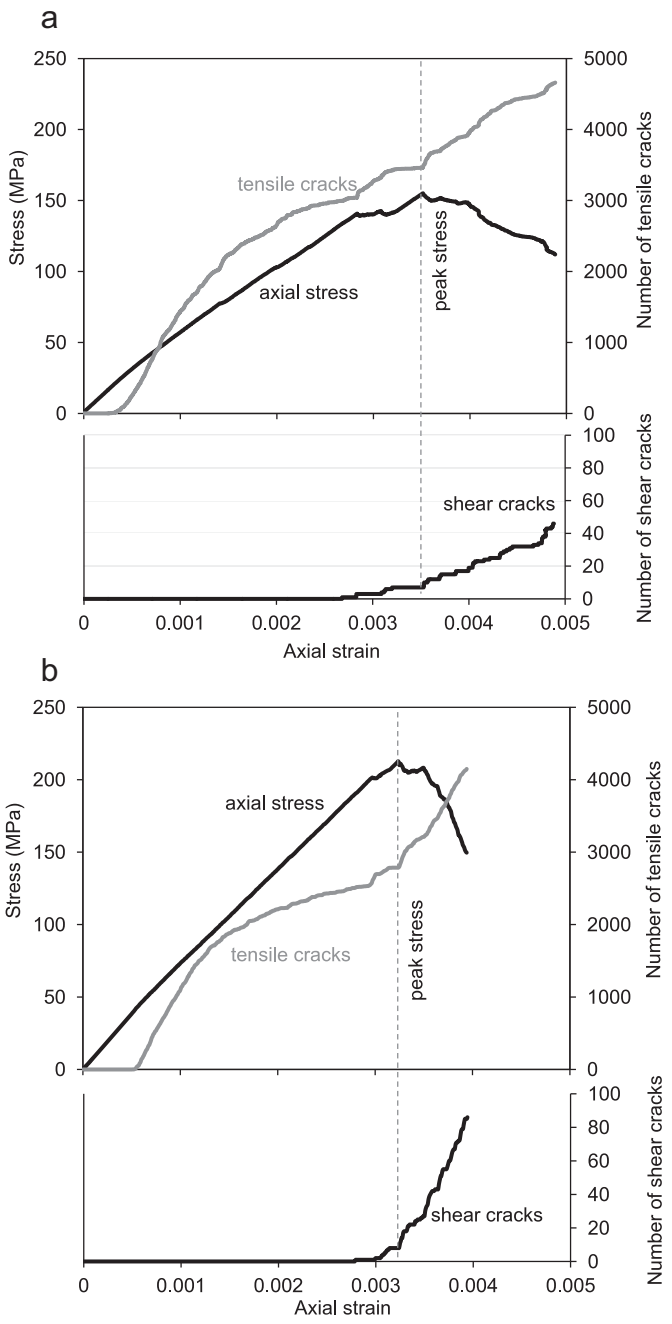

Fig. 8. Stress–strain curves and number of tensile and shear cracks in the damaged clumped specimens from: (a) borehole parallel to the σ_3 direction; and (b) borehole parallel to the σ_1 direction.

initial crack density and crack geometry. As mentioned earlier, the damaged clumped specimen fails to capture the initial non-linear section of the stress–strain curve because cracks were not sufficiently opened during the unloading stages. Once the cracks are closed, the rock behaves in a linear elastic manner (Stage 2) until the crack initiation (*CI*) stress, which marks the beginning of Stage 3 with stable crack growth. At this stage, cracks are generated parallel to the loading direction and this is reflected by the onset of nonlinearity of the lateral strain curve. The plot of lateral strain versus axial strain can therefore be used to identify the *CI* stress; it is defined as the point of deviation from linear elasticity. The magnitude of axial stress where the volumetric strain reversal occurs marks the beginning of unstable crack growth (Stage 4). This point usually occurs between 70% and 85% of the peak

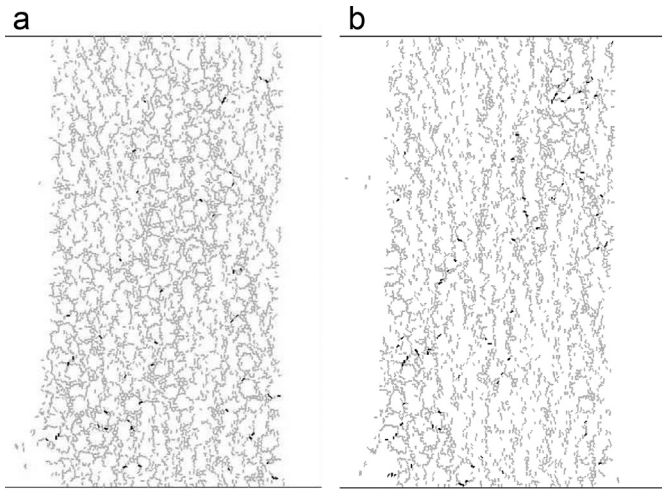

Fig. 9. (a) micro-cracks generated from the beginning of the test up to 70% of the peak in the post-peak region, in the case of the borehole parallel to the σ_3 direction; (b) micro-cracks generated from the beginning of the test up to 70% of the peak stress in the post-peak region, in the case of a borehole parallel to the σ_1 direction. Gray and black lines in (a) and (c) indicate tensile and shear cracks, respectively.

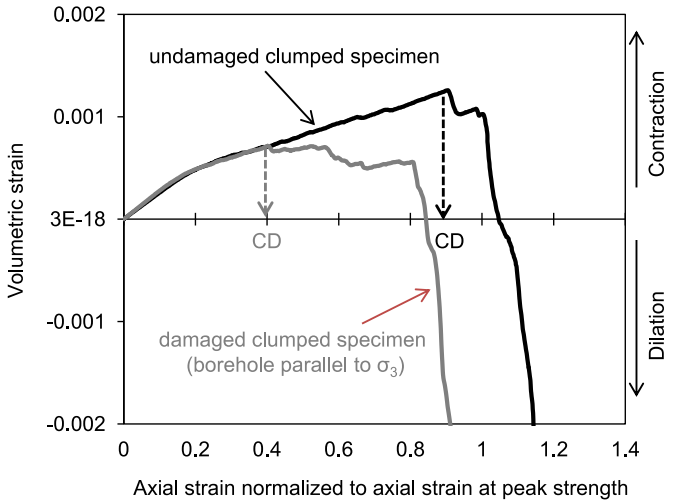

Fig. 10. Comparison of volumetric strain versus axial strain curves for the undamaged clumped specimen (black curve) and damaged clumped specimens from the boreholes parallel to the σ_3 directions (gray curve).

strength and is called the crack damage (*CD*) stress. The plot of volumetric strain versus axial strain can be used to identify both the *CI* and *CD* stresses.[20]

It was found that the value of *CI* stress is independent of the amount of damage; the values of *CI* stress for the undamaged and damaged clumped specimens were determined to be about 21% and 24% of their peak strengths, respectively. Eberhardt et al.[5] found that the degree of sample disturbance had only minor effect on the *CI* stress. However, the clumped specimens were found to underestimate the values of *CI* stress for both undamaged and damaged *LdB* granite by a factor of about two; the *CI* stresses of the undamaged and damaged clumped specimens were calculated to be 44 ± 2 MPa and 38 ± 4 MPa, respectively, whereas the *CI* stresses for the undamaged and damaged *LdB* granite were reported by Eberhardt et al.[5] to be 82 ± 4 MPa and 76 ± 2 MPa, respectively. The underestimation of the *CI* stress by the clumped particle model could be due to the rigidness of the unbreakable and irregular-shaped clumps, which results in the generation of large moments and tensile stresses and the formation of tensile cracks at early loading stages. It is anticipated that a better match with the *CI* stress of *LdB* granite can be achieved by increasing the bond tensile strength and recalibrating the *UCS* (i.e., reducing the bond shear strength). Such a model would however overestimate the tensile strength as was the case in the clumped particle model calibrated to the *UCS* and the *CI* stress of Aue granite by Yoon et al.[32]

Fig. 10 shows the volumetric strain versus the axial strain normalized to its value at the peak strength for the undamaged and damaged clumped specimens (from the boreholes parallel to the σ_3 directions). In the undamaged clumped specimen, the volumetric strain increases monotonically past the *CI* stress with a constant slope as the axial strain increases. The volumetric strain reversal occurs at about 90% of the intact *UCS*, which corresponds to the onset of shear cracks in the clumped specimen. In the damaged clumped specimen from the borehole parallel to the σ_3 direction, the volumetric strain curve becomes nonlinear past the *CI* stress at about 40% of its *UCS*. From this point forward, which is regarded as the *CD* stress, the volumetric strain reverses its direction and gradually decreases until 0.8*UCS*, where an abrupt reduction in the volumetric strain occurs.

It was found that the values of *CD* stress for the undamaged and damaged clumped specimens (from the borehole parallel to the σ_3 direction) correspond with those of *LdB* granite reported by Eberhardt et al.;[5] the *CD* stresses of the undamaged and damaged clumped specimens were calculated to be 167 ± 39 MPa and 109 ± 24 MPa, respectively, and the *CD* stresses for the undamaged and damaged *LdB* granite were reported by Eberhardt et al.[5] to be 156 ± 13 MPa and 100 ± 12 MPa, respectively. Therefore, the clumped particle model captures the observed reduction in the average *CD* stress from the undamaged to damaged specimens (Fig. 10). As explained by Eberhardt et al.,[5] in a highly damaged rock, the stress–relief cracks provide weak paths from which active cracks may propagate more easily. This results in a lower *CD* stress as well as a lower peak strength of the highly damaged rock compared with that of the undamaged or moderately damaged rock.

4. Conclusion

Drilling in a high stress environment may result in core damage in the form of micro-cracks. The drilling-induced core damage has been known to influence the mechanical properties of rock specimens measured in the laboratory. In this study, continum and discontinum codes were used to investigate the influence of stress path (i.e., borehole orientation) on drilling-induced core damage. The analyses using the 3D elastic *FEM* code, Abaqus, showed that a core may experience a complex stress path during drilling, which involves stress increase, decrease and rotation. The details of the stress path depends of the borehole orientation.

The approximate 3D coring stress paths of the boreholes parallel to the σ_1 and σ_3 directions within a stress state representative for the 420-level of the *URL* were applied to a *PFC2D* clumped specimen previously calibrated to the laboratory properties of undamaged *LdB* granite. The following conclusions are made:

(1) Micro-cracks in the simulated core retrieved from the borehole parallel to the σ_3 direction are oriented nearly perpendicular to the specimen axis; (2) micro-cracks in the simulated core retrieved from the borehole parallel to the σ_1 direction are oriented sub-parallel to the specimen axis; (3) the simulated core retrieved from the borehole parallel to the σ_3 direction contains more micro-cracks than that retrieved from the borehole parallel to the σ_1 direction; (4) the simulated core retrieved from the borehole parallel to the σ_3 direction are weaker and softer than that retrieved from the borehole parallel to the σ_1 direction; (5) the clumped particle model underestimates the crack initiation

stress when calibrated to the *LdB* granite unconfined compressive and direct tensile strengths; (6) in the clumped particle model, unloading-induced micro-cracks do not influence the crack initiation stress; (7) the clumped particle model captures the crack damage stress when calibrated to the *LdB* granite unconfined compressive and direct tensile strengths; and (8) in the clumped particle model, unloading-induced cracks reduce the crack damage stress.

The use of a modeling technique that simulates damage initiation and accumulation, here a clumped particle model in *PFC2D*, allows for capturing most of the observed effects summarized above. The following modifications may enhance the modeling results:

(1) Application of a more realistic stress path considering both deviatoric and tensile stresses, as well as stress rotation that occurs during coring process; (2) calibration of the clumped particle model to the crack initiation stress rather than the tensile strength; (3) use of the *PFC2D* grain-based model[33,34] with breakable and deformable grains; and (4) simulation of actual drilling process using a three-dimensional code based on the distinct element method (e.g., *PFC3D*[35]).

The numerical simulation results presented in this paper suggest that the rock strength measured in the laboratory on samples retrieved from high stress fields should be treated with caution. Other methods of rock strength evaluation such as borehole geophysics and back analysis of borehole breakouts along with laboratory testing may deliver more reliable estimates of the in situ intact rock strength. The analysis results reported here confirm the effect of sample disturbance on mechanical properties of rocks measured in the laboratory and potentially offers a possible approach to simulate this process and quantify the drilling-induced core damage.

Acknowledgments

This research project was supported by the Rio Tinto Centre for Underground Mine Construction at *CEMI*, Natural Sciences and Engineering Research Council of Canada (*NSERC*) and Itasca Consulting Group. The authors would like to thank Erik Eberhardt and Derek Martin for many insightful discussions and providing the *LdB* granite laboratory test data. The technical advice on the *PFC* numerical simulations received from David Potyondy, Matthew Pierce and Sacha Emam from Itasca is thankfully acknowledged.

References

1. Martin CD, Stimpson B. The effect of sample disturbance on the laboratory properties of Lac du Bonnet granite. *Can Geotech J.* 1994;31:692–702.
2. Martin CD, Christiansson R. Overcoring in highly stressed granite-the influence of microcracking. *Int J Rock Mech Min Sci Geomech Abstr.* 1991;28(1)53–70.
3. Lavrov A. The Kaiser effect in rocks: principles and stress estimation techniques. *Int J Rock Mech Min Sci.* 2003;40:151–171.
4. Jaeger JC, Cook NGW. Pinching-off and discing of rocks. *J Geophys Res.* 1963;68:1759–1765.
5. Eberhardt E, Stead D, Stimpson B. Effects of sample disturbance on the stress-induced microfracturing characteristics of brittle rock. *Can Geotech J.* 1999;36:239–250.
6. Watson BP, Kuijpers JS, Henry G, Palmer CE, Ryder JA. Nonlinear rock behaviour and its implications for deeper level platinum mining. *J S Afr Inst Min Metall.* 2009;108:5–13.
7. Lanaro F, Sato T, Nakama S. Depth variability of compressive strength test results of Toki granite from Shobasama and Mizunami Construction Sites, Japan. *Rock Mech Rock Eng.* 2009;42:611–629.
8. Holt RM, Brignoli M, Kenter CJ. Core quality: quantification of coring-induced rock alteration. *Int J Rock Mech Min Sci.* 2000;37:889–907.
9. Holt RM, Brandshaug T, Cundall PA. Discrete particle and laboratory modeling of core mechanics, In: Girard J, Liebman M, Breeds C, Doe T (Eds.). *Proc. of the 4th North American Rock Mech Symposium*. Seattle: AA Balkema, Rotteram; 2000: pp. 1217–1224.
10. Holt RM, Pestman BJ, Kenter CJ. Use of a discrete particle model to assess feasibility of core based stress determination, In: Elsworth D, Tinucci JP, Heasley KA (eds.). Rock mechanics in the national interest, vol 2, *Proceedings of the 38th US Symposium Rock Mechanics*. Washington DC: Swers & Zeitlinger, Lisse: 2001: pp. 1361-66.
11. Holt RM, Doornhof D, Kenter CJ. Use of discrete particle modeling to understand stress-release effects on mechanical and petrophysical behavior of granular rocks. In: Konietsky H, editor. *Numerical Modeling in Micromechanics via Particle Methods.* Lisse: Swers & Zeitlinger; 2003. p. 269–276.
12. Gorodkov S, Li L, Holt RM. Stress path during coring: a discrete particle modeling approach. In: Lu M, Li CC, Kjorholt H, Dahle H, editors. *In-situ Rock Stress.* London: Taylor and Francis Group; 2006. p. 541–549.
13. Zang A, Stephansson O. *Stress Field of Earth's Crust.* Berlin: Springer; 2010.
14. Li Y, Schmitt DR. Effects of Poisson's ratio and core stub length on bottomhole stress concentrations. *Int J Rock Mech Min Sci.* 1997;34:761–773.
15. Corthésy R, Leite MH. A strain-softening numerical model of core discing and damage. *Int J Rock Mech Min Sci.* 2008;45:329–350.
16. Valley B, Bahrani N, Kaiser PK. Rock strength obtained from core samples and borehole wall instabilities – the effect of drilling induced damage. In: Zhao J, Labiouse V, Dudt J-P, Mathier J-F (eds.). Rock Mechanics in Civil and Environmental Engineering. *Proc. of the European Rock Mechanics Symposium (EUROCK)*. Lausanne, Switzerland. Leiden: CRC Press/Balkema; 2010: pp. 331-334.
17. Obert L, Stephenson DE. Stress conditions under which core discing occurs. *Trans Soc Min Eng Am Inst Min Eng.* 1965;232(3)227–235.
18. Martin CD. Characterizing in situ stress domains at the AECL Underground Research Laboratory. *Can Geotech J.* 1990;27:631–646.
19. Martin CD, Read RS. AECL's mine by experiment: a test tunnel in brittle rock. In: *Proceedings of the 2nd North American Rock Mechanics Symposium*, vol. 1. Montreal; 1996: pp. 13–24.
20. Martin C. *The Strength of Massive Lac du Bonnet Granite Around Underground Openings.* Canada: University of Manitoba; 1993. p. 278 PhD thesis.
21. Eberhardt E. Personal communication. 2010.
22. Lim SS, Martin CD. Core disking and its relationship with stress magnitude for Lac du Bonnet granite. *Int J Rock Mech Min Sci.* 2010;47:254–264.
23. Itasca, *Particle Flow Code in 2 Dimensions (PFC2D)*, 2008, Itasca Consulting Group Inc., Minneapolis Ver 4.0.
24. Cundall PA. A computer model for simulating progressive, large scale movements in blocky rock systems. In: *Proc. Symposium of the International Society for Rock Mechanics*. Nancy; 1971: No. 8.
25. Cundall PA, Strack ODL. A discrete numerical model for granular assemblies. *Geotechnique.* 1979;29(1)47–65.
26. Potyondy DO, Cundall PA. A bonded particle model for rock. *Int J Rock Mech Min Sci.* 2004;41:1329–1364.
27. Martin CD, Chandler NA. The progressive fracture of Lac du Bonnet granite. *Int J Rock Mech Min Sci Geomech Abstr.* 1994;31(6)643–659.
28. Hajiabdolmajid V, Kaiser PK, Martin CD. Modelling brittle failure of rock. *Int J Rock Mech Min Sci.* 2002;39(6)731–741.
29. Holt RM, Kjølaas J, Larsen I, Li L, Gotusso Pillitteri A, Sønstebø EF. Comparison between controlled laboratory experiments and discrete particle simulations of the mechanical behavior of rock. *Int J Rock Mech Min Sci.* 2005;42:985–995.
30. Cho N, Martin CD, Sego DC. A clumped particle model for rock. *Int J Rock Mech Min Sci.* 2007;44:997–1007.
31. Diederichs MS. *Instability of Hard Rockmass: The Role of Tensile Damage and Relaxation [PhD thesis].* Canada: University of Waterloo; 1999 567p.
32. Yoon JS, Zang A, Stephansson O. Simulating fracture and friction of Aue granite under confined asymmetric compressive test using clumped particle model. *Int J Rock Mech Min Sci.* 2012;49:68–83.
33. Potyondy DO. A grain-based model for rock: approaching the true microstructure. In: *Proc. of the Rock Mechanics in the Nordic Countries* ; 2010: 10p.
34. Bahrani N, Kaiser PK, Valley B. Distinct element method simulation of an analogue for a highly interlocked, non-persistently jointed rockmass. *Int J Rock Mech Min Sci.* 2014;71:117–130.
35. Itasca. *Particle Flow Code in 3 Dimensions (PFC3D).* Minneapolis: Itasca Inc.; 2008 Version 4.0.